Ocean Engineering 306 (2024) 118008

Contents lists available at ScienceDirect

Ocean Engineering

journal homepage: www.elsevier.com/locate/oceaneng

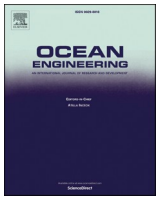

Research paper

Fluid structure interaction analysis of counter flow in a partially layered vertical channel of double deformable passages

Muneer Ismael [a,b,*], Mohammad Ghalambaz [c,d], Zehba Raizah [e], Mehdi Fteiti [f]

[a] Mechanical Engineering Department, Engineering College, University of Basrah, Basra, Iraq
[b] College of Engineering, University of Warith Al-Anbiyaa, Karbala, Iraq
[c] College of Engineering, Almaaqal University, Basra, 61003, Iraq
[d] Laboratory on Convective Heat and Mass Transfer, Tomsk State University, 634045, Tomsk, Russia
[e] Department of Mathematics, Faculty of Science, King Khalid University, Abha, 62529, Saudi Arabia
[f] Physics Department, Faculty of Applied Science, Umm Al-Qura University, Makkah, 24381, Saudi Arabia

ARTICLE INFO

Keywords:
Double-passage
Vertical channel
FSI
Porous
Flexible wall
Strained wall

ABSTRACT

Cooling of two parallel surfaces with different temperatures is encountered in marine equipment. This requires a compact heat exchanger of two separated fluids, which counts on the double-passage channel. The present study uses a flexible separator to isolate two vertical passages, each partially filled with a porous layer. The permeability of the porous layers (Darcy number, Da), Reynolds number of each passage, temperature ratio, and the modulus of elasticity of the separator are scrutinized. Finite element method with the coupled ALE approach is employed in the numerical treatises. Results show that the strain energy of the elastic separator promotes the overall performance of the heat transfer, where at Da $= 10^{-4}$, the left wall Nusselt number elevates by 10.4% and that of the right wall by 16.25% when the separator is changed from rigid to a flexible one. As the porous layers meet high permeability, energy transfer from the hot surfaces to the cold fluid upgrades notably, where the Nusselt number increases by 138% for the left wall and 96% for the right wall when Da is increased from 10^{-5} to 10^{-1}. It is found in a high permeable layer, the flexible separator showcases higher performance than the rigid separator.

Nomenclature

C_f	Forchheimer drag coefficient	***Greek symbols***	
Da	Darcy number	α_r	Ratio of the thermal diffusivity
DPC	Double-passage channel	β	Coefficient of the thermal expansion
ds	Displacement of the coordinate, vector	ΔP	Pressure drop
E	Modulus of elasticity, dimensionless	θ	Temperature, dimensionless
E*	Modulus of elasticity, dimensional	ε	Porosity
f	Friction factor	ρ	Density
F_V	Body force term in the flexible separator	σ	Stress tensor
Gr	Grashof number	φ	Index for fixed and deformed domains
g	Gravitational acceleration	λ	Index for porous, clear passages
H	Length of the channel	***Subscripts***	
k	Thermal conductivity	av	Average
K	Permeability of the porous layers	c	Cold
n	Normal vector	eff	Effective
Nu	Nusselt number	f	fluid
P	Fluid pressure	h1	Hot left wall
PEC	Performance criterion	h2	Hot right wall
Pr	Prandtl number	j	Index of a passage
r_T	Temperature ratio	in	Inlet
Re	Reynolds number	L	Left
Ri	Richardson number	Max.	Maximum
T	Temperature, dimensional	o	Reference solid separator
t	Time, dimensionless	R	Right
t*	Time, dimensional	r	Ratio

(*continued on next column*)

(*continued*)

(*continued on next page*)

* Corresponding author. Mechanical Engineering Department, Engineering College, University of Basrah, Basra, Iraq.
E-mail addresses: muneer.ismael@uobasrah.edu.iq (M. Ismael), m.ghalambaz@gmail.com (M. Ghalambaz), zaalrazh@kku.edu.sa (Z. Raizah), mafteiti@uqu.edu.sa (M. Fteiti).

https://doi.org/10.1016/j.oceaneng.2024.118008
Received 7 October 2023; Received in revised form 18 April 2024; Accepted 22 April 2024
Available online 4 May 2024

(*continued*)

U,V	Fluid velocity components	s	Solid
Us, Vs	Coordinates velocity components	sm	Solid matrix
w	Passage width	I, II, III, IV	Passage index
x, y	Cartesian coordinates		

1. Introduction

In the intricate domain of heat exchange technologies, the pursuit of efficiency never ceases. Creating effective, compact, and reliable heat exchangers is not just an academic endeavor; it is a critical requirement for many engineering and domestic applications. Double-passage channel (DPC) flow is a specific architecture, which holds promise for redefining benchmarks in heat exchange efficiency and adaptability (Ghalambaz et al., 2021; Slimani et al., 2015).

Traditionally, cooling two parallel surfaces possessing different temperatures calls for a specialized heat exchanger capable of isolating two separated fluids. This need becomes especially salient in DPC flow, a configuration geared towards the proficient interchange of thermal energy. The significance of DPC flow is underscored by its pivotal role in a diverse range of applications, from the channeled blades in gas turbines (Obata et al., 1989) to microchannels and sinks in electronic cooling systems (Umavathi et al., 2017), solar collectors (Salah El-Din, 2001), and oil-water radiators in internal combustion engines (Vijayaraghavan et al., 2022), where most, if not all, of these applications are encountered in marine equipment.

The merit of DPC flow primarily stems from its capacity to enhance heat transfer by expanding the surface area available for the thermal interaction between fluids. However, even this promising technology offers room for advancement and innovation. This is where the concept of "deformable passages" enters the scene. Unlike traditional DPC flow configurations, this novel approach incorporates an added layer of complexity by featuring deformable passages (Ismael et al., 2022). The inclusion of deformability not only grants adaptive heat transfer capabilities but also boosts the effective surface area, thereby creating new opportunities for performance enhancement.

Utilizing porous media, particularly metal foams, has emerged as a game-changing strategy to augment channel heat transfer. Metal foams have become prominent in heat exchanger designs courtesy of their unparalleled thermal and hydrodynamic attributes. Boasting exceptional porosity and remarkable surface area-to-volume ratios, these materials are under intensive study for their ability to elevate heat transfer rates while keeping pressure drops within manageable levels. Several researches examined using porous materials in channels. For example, the concept of entropy generation and exergy in partially filled metal foams was investigated in (Ismael et al., 2022). In the investigation, aluminum metal foam characterized by a pore density of 10 and a porosity of 0.95 was employed to probe the impact of different foam thicknesses and filling rates. The study found that partially filled metal foams were superior to fully-filled ones in metrics such as entropy generation and exergy transfer. To accurately model both fluid flow and heat transfer behaviors, the local thermal non-equilibrium (LTNE) model along with the Darcy extended Forchheimer (DEF) model were utilized.

While the focus on single-metal foams has been beneficial, advancements have been made in utilizing functionally graded metal foams, particularly aluminum and copper (Jadhav et al., 2023). Different configurations were studied under partially filled conditions, employing DEF and LTNE models. Interestingly, the research revealed that decreasing graded foam led to higher heat transfer rates while simultaneously reducing pumping power requirements by up to 84%. Optimization studies have been imperative in ascertaining the ideal

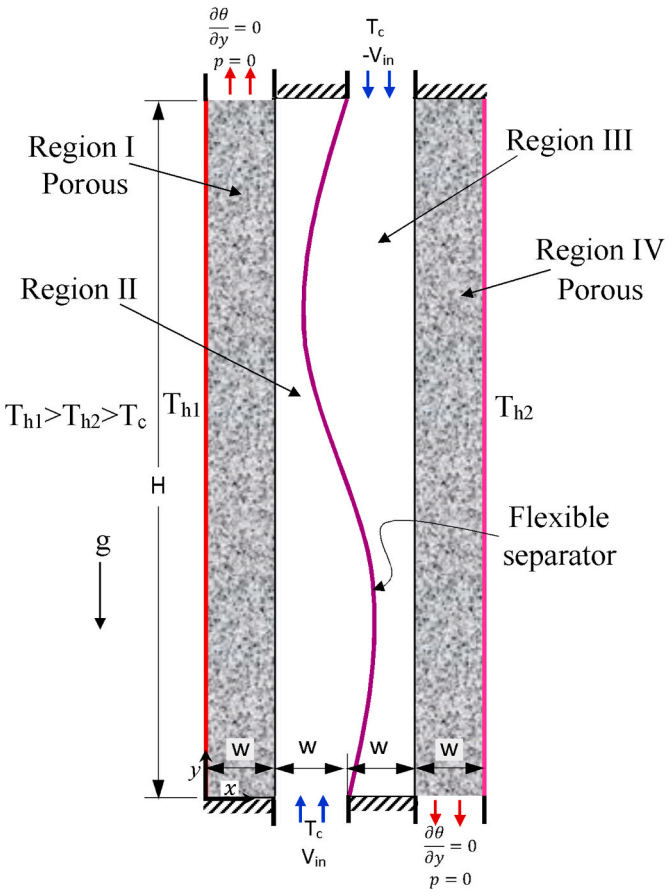

Fig. 1. Schematic description of the physical problem.

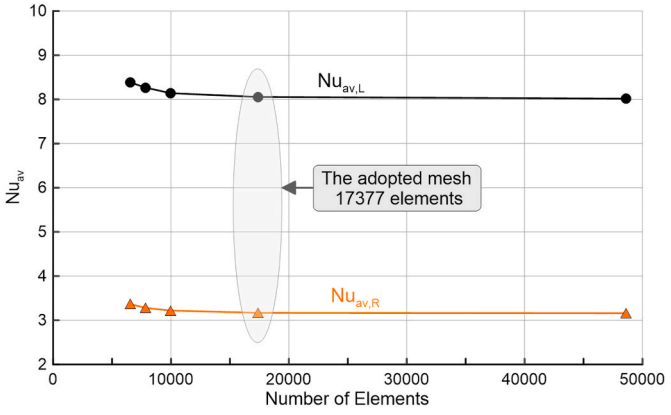

Fig. 2. Assessment of the mesh independence based on the Nusselt number over the right and left walls for $Re_{II} = 200$, $Re_{III} = 300$, $Da = 10^{-4}$, $E = 10^{5,}$ and $r_T = 0.4$.

structural parameters for metal foams, simultaneously improving heat transfer and mitigating pressure drop (Jadhav et al., 2022). A multi-objective optimization was employed using TOPSIS techniques, concluding that an aluminum foam with 80% filling and pore density of 30 PPI provided the best performance score when equal importance was accorded to heat transfer and friction effects. Computational methodologies, including genetic algorithms and artificial neural networks, have also been applied for heat transfer optimization in heat exchangers with different metal foams (Athith et al., 2022). The storage and conversion of energy can be done perfectly by implementing multiscale architected porous materials (Hoseini et al., 2023).

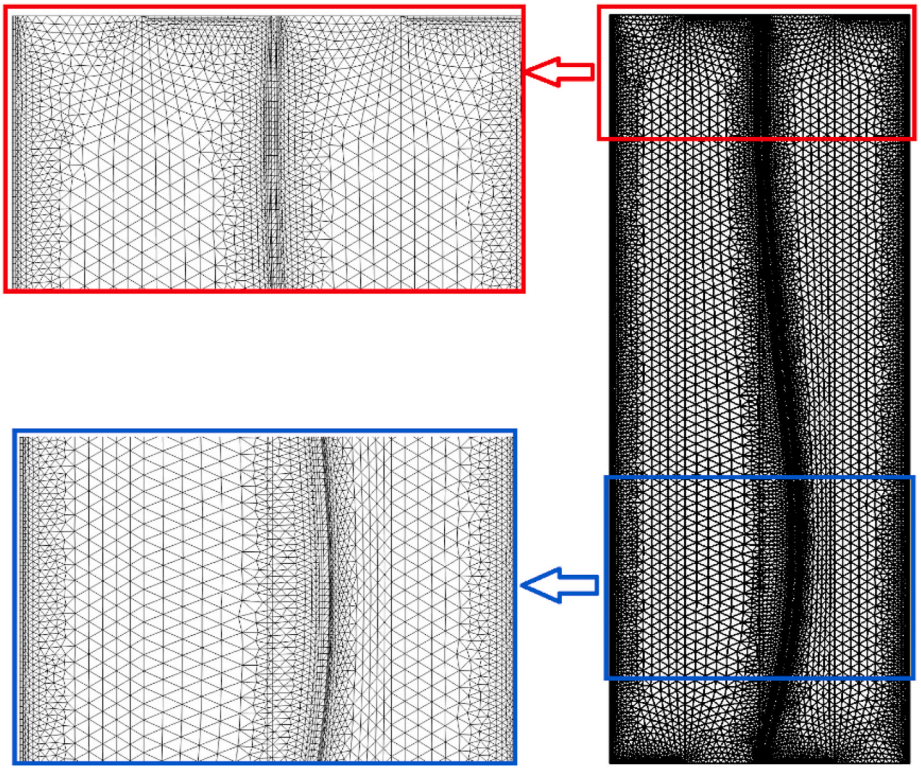

Fig. 3. Distribution of 17,377 elements deforming within regions II and IV.

Table 1
Assessment of the mesh independence based on the Nusselt number over the right and left walls for $Re_{II} = 200$, $Re_{III} = 300$, $Da = 10^{-4}$, $E = 10^{5,}$ and $r_T = 0.4$

No. Of elements		6556		7846		9954		17,377		48,625	
$Nu_{av,\ L}$	Error	8.383	–	8.267	1.4%	8.140	1.6%	8.054	1.0%	8.016	0.5%
$Nu_{av,\ R}$	Error	3.365	–	3.280	2.6%	3.220	1.9%	3.168	1.6%	3.160	0.3%

Table 2
Validation of the local Nusselt number with the analytical study of double-passage vertical flow, Salah El-Din (2001)

Y*	*Nu* at y = b, $x = 0.5\ b$		Error
	Numerical	Salah El-Din (2001)	
0.6	5.39	5.23	3%
0.8	10.19	10.20	0.09%

Further enhancements have been attempted through novel design modifications, such as varying foam filling heights and tilt angles in heat sinks filled with nanofluids (Chen et al., 2022). Experiments revealed that a metal foam filling height of 6 mm showed the best comprehensive performance, while tilt angles adversely affected cooling performance. The shape of the metal foam layer itself was demonstrated to dramatically influence thermal charging response times in latent heat thermal energy storage systems (Fteiti et al., 2023). Modifications in the geometry of the foam layer can influence storage capacity by approximately 60%, underscoring the critical nature of thoughtful design choices. Lastly, the incorporation of periodic vertical porous ribs in microchannel heat sinks has been shown to drastically improve the Nusselt number while maintaining lower pressure drops compared to solid ribs (Lori and Vafai, 2022).

Biswas et al. (2020a, 2020b) suggested an alternative tool to enhance the natural convection inside a space involving a block heater mounted on the middle of the bottom wall. This tool was by aspiring a coolant through vents located on the base and the roof of the space. They indicated a prominent enhancement with this strategy which consumes zero power in both clear space (Biswas et al., 2020b) and porous space (Biswas et al., 2020a). Biswas et al. (2015) discussed the segmental heating on the sides of a ventilated space. The salient result was the feature of the segmental heating over the whole side heating. Then, the problem is upgraded by Hazra et al. (2020) using corner heaters and filling the space with a porous medium while applying a transverse magnetic field. The effect of the magnetic field was common in suppressing the heat transfer while the porosity of the medium provided more free passages to flow and hence enhanced the Nusselt number.

Flow and heat transfer in double-passage channels have garnered significant attention due to their wide applications in fields ranging from chemical engineering to thermal management systems. Advancements in computational fluid dynamics (CFD) have provided invaluable insights into optimizing heat transfer efficiency in such complex geometries. This article aims to delve into the fundamental aspects of flow and heat transfer in double-passage channels, drawing primarily from the recent research contributions in the domain. A common method for heat exchange in double-passage channels involves using concentric tube heat exchangers, typically in chemical and food processes (Lori and Vafai, 2022). Recent simulations show that spherical dimpled tubes could significantly increase the overall heat transfer coefficient, effectiveness, and heat transfer rate compared to plain tubes (Lori and Vafai, 2022). Parameters such as velocity, Nusselt number, pressure drop, and friction factor were evaluated, highlighting the utility of CFD in complex heat transfer studies. Research has also explored the impact of an electrically conducting fluid in a vertical double-passage channel (Umavathi et al., 2017). By maintaining constant yet different temperatures and

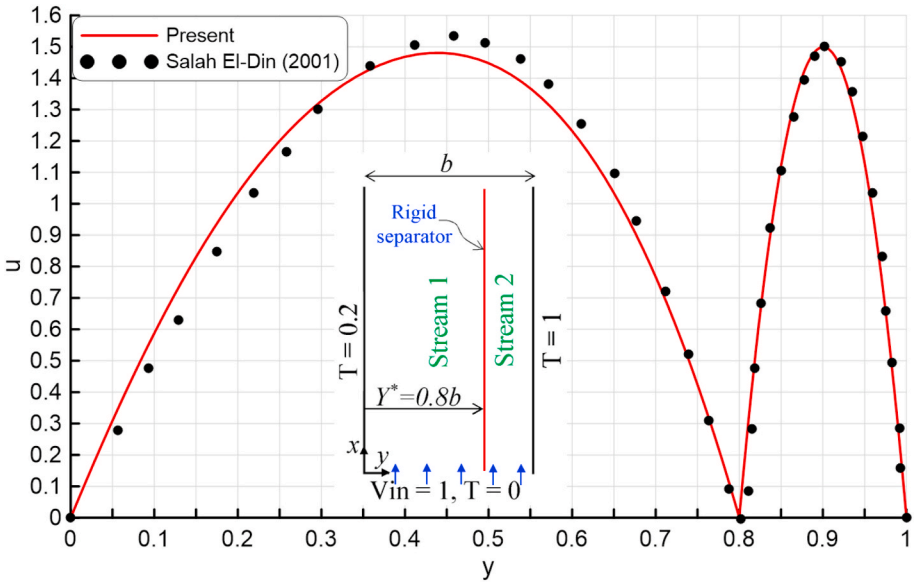

Fig. 4. Comparison of the vertical velocity component in a double-passage vertical channel, Salah El-Din (2001).

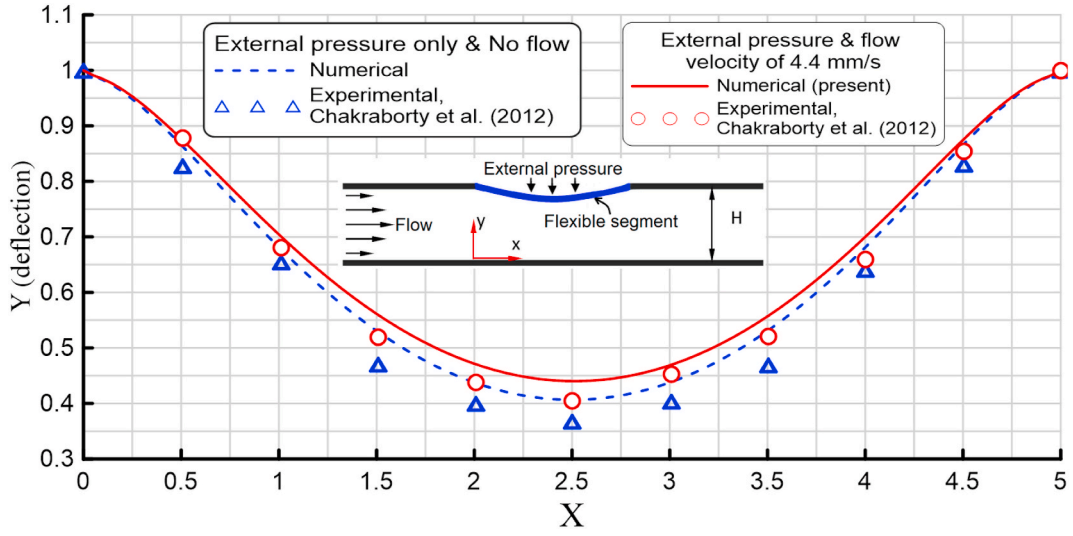

Fig. 5. Validating the FSI solution with experimental results of the horizontal channel of a partly elastic slice.

concentrations at the wall and the ambient medium, the authors observed the effects of various parameters such as thermal Grashof number, Brinkman number, and Hartmann number. It was found that certain parameters enhanced flow while others suppressed it, indicating an intricate balance of factors affecting both heat and mass transfer. The complexity of double-passage channels is not restricted to fluid types or geometrical considerations alone. The flow of Walter's fluid and the introduction of a heat source in a wavy channel offers another layer of complexity (Kumar et al., 2011). Here, variations in physical parameters like baffle position and Grashof number affected both the velocity and temperature fields.

Regarding laminar convection, a perfectly conducting thin plane baffle dividing the channel was found to affect the value of Nusselt number based on its position (Salah El-Din, 1994). Studies have also scrutinized the impact of viscous dissipation on laminar mixed convection, revealing that variations in the Brinkman number produce divergent effects on the Nusselt number at hot and cold wall surfaces (Salah El-Din, 2002). While horizontal channels have received comparatively less attention, their importance is no less significant (Cheng et al., 1989). Research indicates that both the baffle's placement and the thermal boundary conditions on the channel walls can substantially alter thermal characteristics. Interestingly, the study extends to porous annuli with a central baffle, considering the effects of parameters like Grashof number, Darcy number, and radius ratio on thermal and velocity fields (Girish et al., 2018). Magnetic fields and first-order chemical reactions add another layer of complexity to the convective heat transfer in double-passage channels (Pratap Kumar et al., 2016; Sankar et al., 2018). A magnetic field was found to alter velocity profiles significantly, and first-order chemical reactions had a noticeable effect on the flow variables. Additionally, the role of viscous dissipation has been explored extensively, providing comprehensive details on how it affects thermal distribution and velocity profiles (Athal et al., 2023; Girish and Sankar, 2020; Sankar et al., 2018).

Considering deformable structures, some recent researchers utilized flexible (deformable) structures in natural or mixed convection flows to improve the fluid flow and heat transfer further. One of the key advantages of a flexible wall over a rigid wall lies in its ability to adjust its shape in response to flow conditions. This change in shape, controlled by

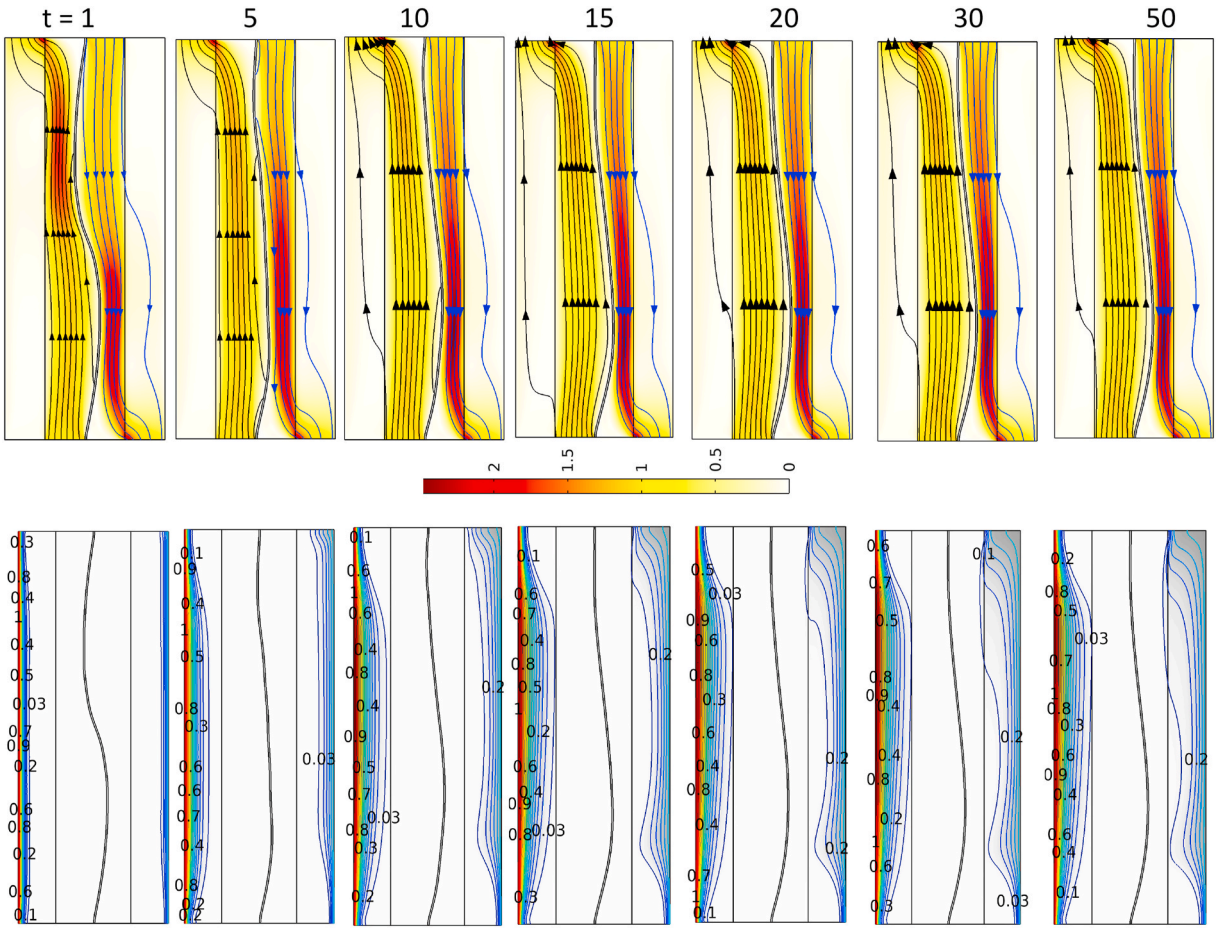

Fig. 6. Progression of the flow and thermal fields with time for $Re_{II} = 200$, $Re_{III} = 300$, $Da = 10^{-4}$, $E = 10^{5,}$ and $r_T = 0.4$.

the elastic modulus of the wall, can serve as a control element for heat transfer rates. The change in shape generates a strain energy in the wall (Pantua et al., 2020). A study of natural convection in a flexible-sided triangular cavity found that local and average heat transfer characteristics were influenced by the elastic modulus of the wall, with a decrease in heat transfer at higher internal Rayleigh numbers and Hartmann numbers. Including an inclined magnetic field was found to reduce convection, especially for higher external Rayleigh numbers (Selimefendigil and Öztop, 2016b). Mixed convection studies in triangular cavities partially filled with nanofluids also reveal that as the value of elastic modulus increases, local and average heat transfer are enhanced. Interestingly, adding nanoparticles to the base fluid improved heat transfer efficiency, especially for lower values of the Richardson number and internal Rayleigh number (Selimefendigil and Öztop, 2017).

The shape of the cavity can also play a role in the management of the energy transfer. In a 3D lid-driven trapezoidal cavity study, it was observed that flexible side surfaces could be used as a control element for the heat transfer rate. The study demonstrated a direct relationship between the elastic modulus of the side surfaces and the heat transfer rate. Additionally, adding nanoparticles to the base fluid resulted in a linear increment of heat transfer (Selimefendigil et al., 2017). Several studies have also investigated the role of magnetic fields in these systems. Generally, increasing the Hartmann number is observed to lead to a deterioration in local and average heat transfer rates (Selimefendigil and Öztop, 2016a; Selimefendigil et al., 2019). These effects become more pronounced with higher Richardson numbers. In such systems, the nanoparticle volume fraction is effective in enhancing heat transfer (Selimefendigil et al., 2019).

The shape and motion of internal elements like cylinders in the enclosure also affect heat transfer. A study incorporating a rotating cylinder in a cavity filled with SiO2–water nanofluids revealed that cylinder rotation enhances average heat transfer for all nanoparticle types (Selimefendigil et al., 2016). One outlier to the efficacy of flexible walls is in a system filled with a porous medium. It was found that including a flexible wall did not significantly improve free convective heat transfer compared to a rigid wall system. Instead, the placement of obstructed objects inside the enclosure was more effective for heat transfer enhancement (Khanafer and Vafai, 2020). Overall, using flexible walls in cavities provides a nuanced but promising approach to control heat transfer. The flexibility allows for dynamic adjustment of the system in response to various parameters.

Innovative research on heat transfer in double-passage channels traditionally employs a rigid baffle for separation. However, a recent study introduced a flexible separator sheet, offering new possibilities for heat transfer enhancement (Ismael et al., 2022). By employing numerical simulations through finite element methods (FEM) and arbitrary Lagrangian-Eulerian approaches, the study examines the influence of various parameters, including Reynolds number, elasticity of the sheet, and wall temperature ratios. Interestingly, results indicate that flexible separators are advantageous over rigid ones in enhancing heat transfer passively. Specifically, a 6% improvement in the Nusselt number was observed in the passage with higher temperatures when using a flexible sheet. It is important to mention that, in certain situations, the use of a flexible sheet led to a threefold increase in pressure drop, causing the thermal performance criterion to fall below one in the warmer channel. Nevertheless, thermal performance stayed viable in the channel exposed to cooler temperatures. (Ismael et al., 2022).

The existing literature establishes that porous materials and metal

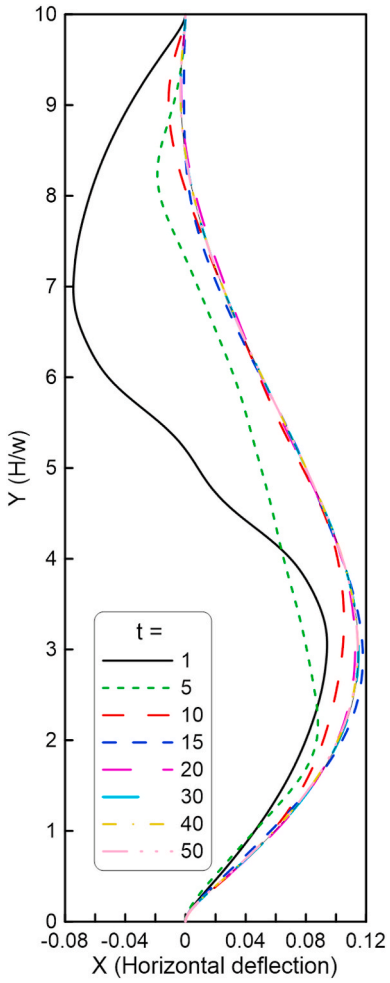

Fig. 7. The profiles of the deforming separator $Re_{II} = 200$, $Re_{III} = 300$, Da = 10^{-4}, E = 10^5 and $r_T = 0.4$.

foams significantly enhance energy transport within channels. Additionally, flexible separators have shown great promise in managing both mixed and natural convection flows, particularly in terms of flow control and heat transfer optimization. Despite this, there is a noticeable gap in research specifically focusing on incorporating flexible separators within channels. Therefore, this study pioneers exploring the effects of utilizing a flexible separator in a double-passage channel incorporating porous layers on its walls. This configuration improves the performance of the energy transport/saving devices as it enhances the thermal energy exchange with lower pressure drop.

2. Mathematical statement

Fig. 1 exemplifies the physical problem of the present paper, which is a vertical channel-comprising counter passages flow separated by a flexible plate. Each passage composed of two layers, a porous layer adjoining the exterior wall and a clear layer adjacent to the flexible separator. The porous medium is preferred in continuous exploitation such as filtration and heat exchanger, thus it is used in this study rather than the metal foam. Consequently, four regions are conceived with a width of w and height of H for each. The flow enters vertically from the clear layer and exits from the porous layer, and this motion occurs upward (positive V_{in}) and downward (negative V_{in}) regarding the left and right passages, respectively. The exterior walls are kept impermeable and heated by T_{h1} and T_{h2}, while the temperature of the entering fluid is the lowest, such that $T_c < T_{h1} < T_{h2}$. The porosity ε and the permeability K of the porous layers are taken the same with a permeable interface with the clear fluid. The heat dissipation and radiation effect are marginal and can be ignored, while the buoyancy effect is taken into consideration due to the counter vertical flow. The separator has a thin thickness with elasticity modulus of E^* and exhibits a relatively very high thermal conductivity to transmit the heat between the passages with lower resistance. Fluid-structure interaction (FSI) is represented by storing the energy in the strained separator and affects the flow through the porous layers. The momentum exchange in porous layers is formulated on the Darcy-Forchheimer model. Furthermore, since the real porous media is composed of a solid matrix, then it is essential in the simulation to keep their geometry unchanged. Therefore, the distortion of the flexible separator is restricted within the clear fluid layers, which deform accordingly. Moreover, the value of the porosity is kept much lower than 0.9 to ensure the local thermal equilibrium (LTE). Hence, the mathematical statement of the current study is casted as in the following non-dimensional equations (Lori and Vafai (2022)), (Hassan and Ismael (2023)).

2.1. Mass conservation

$$\frac{\partial U_j}{\partial X}+\frac{\partial V_j}{\partial Y}=0 \tag{1}$$

2.2. Momentum conservation in x-direction

$$\frac{\partial U_j}{\partial t}+\left(\left(U_j-\varphi Us_j\right)\frac{\partial U_j}{\partial X}+\left(V_j-\varphi Vs_j\right)\frac{\partial U_j}{\partial Y}\right)=-\left(1+\lambda\left(\varepsilon_j^2-1\right)\right)\frac{\partial P_j}{\partial X}$$
$$+\frac{1+\lambda\left(\varepsilon_j-1\right)}{Re_j}\left(\frac{\partial^2 U_j}{\partial X^2}+\frac{\partial^2 U_j}{\partial Y^2}\right)-\lambda\varepsilon_j^2\left(\frac{1}{Re_j Da_j}U_j+\frac{C_f}{\sqrt{Da_j}}|\mathbf{U}_j|U_j\right) \tag{2}$$

Generally, the left hand side terms refer to; unsteady state variation and convective term, respectively. While, the right hand side terms refer to; external surface pressure, diffusive term and the Darcy-Forchhiemer drag imparted by the porous layer. The subscript j is switching among the fourth passages where j = I, IV for the left and right porous passages and j = II, III for the left and right clear passages, as shown in Fig. 1. U is the horizontal fluid velocity and Us is the horizontal velocity of the moving coordinates. The porosity $\varepsilon_j = 0$ for clear domains, II and III.

2.3. Momentum conservation in y-direction

$$\frac{\partial V_j}{\partial t}+\left(\left(U_j-\varphi Us_j\right)\frac{\partial V_j}{\partial X}+\left(V_j-\varphi Vs_j\right)\frac{\partial V_j}{\partial Y}\right)=$$
$$-\left(1+\lambda\left(\varepsilon_j^2-1\right)\right)\frac{\partial P_j}{\partial Y}+\frac{1+\lambda\left(\varepsilon_j-1\right)}{Re_j}\left(\frac{\partial^2 V_j}{\partial X^2}+\frac{\partial^2 V_j}{\partial Y^2}\right)$$
$$-\lambda\varepsilon_j^2\left(\frac{1}{Re_j Da_j}V_j+\frac{C_f}{\sqrt{Da_j}}|\mathbf{U}_j|V_j\right)+Ri_j\theta_j \tag{3}$$

The last term of equation (3) stands for the buoyancy force in all passages, acting vertically.

2.4. Energy conservation

$$\frac{\partial \theta_j}{\partial t}+\left(U_j-\varphi Us_j\right)\frac{\partial \theta_j}{\partial X}+\left(V_j-\varphi Vs_j\right)\frac{\partial \theta_j}{\partial Y}=\frac{(1+\lambda(Kr-1))}{Re_j\,Pr_j}\left(\frac{\partial^2\theta_j}{\partial X^2}+\frac{\partial^2\theta_j}{\partial Y^2}\right) \tag{4}$$

The momentum conservation of the elastic separator is characterized by (Lori and Vafai (2022)):

$$\frac{E}{\rho_r}\frac{\partial^2 \mathrm{ds}}{\partial \mathrm{t}^2}=\nabla\sigma_s+\boldsymbol{F}_\mathrm{v} \tag{5}$$

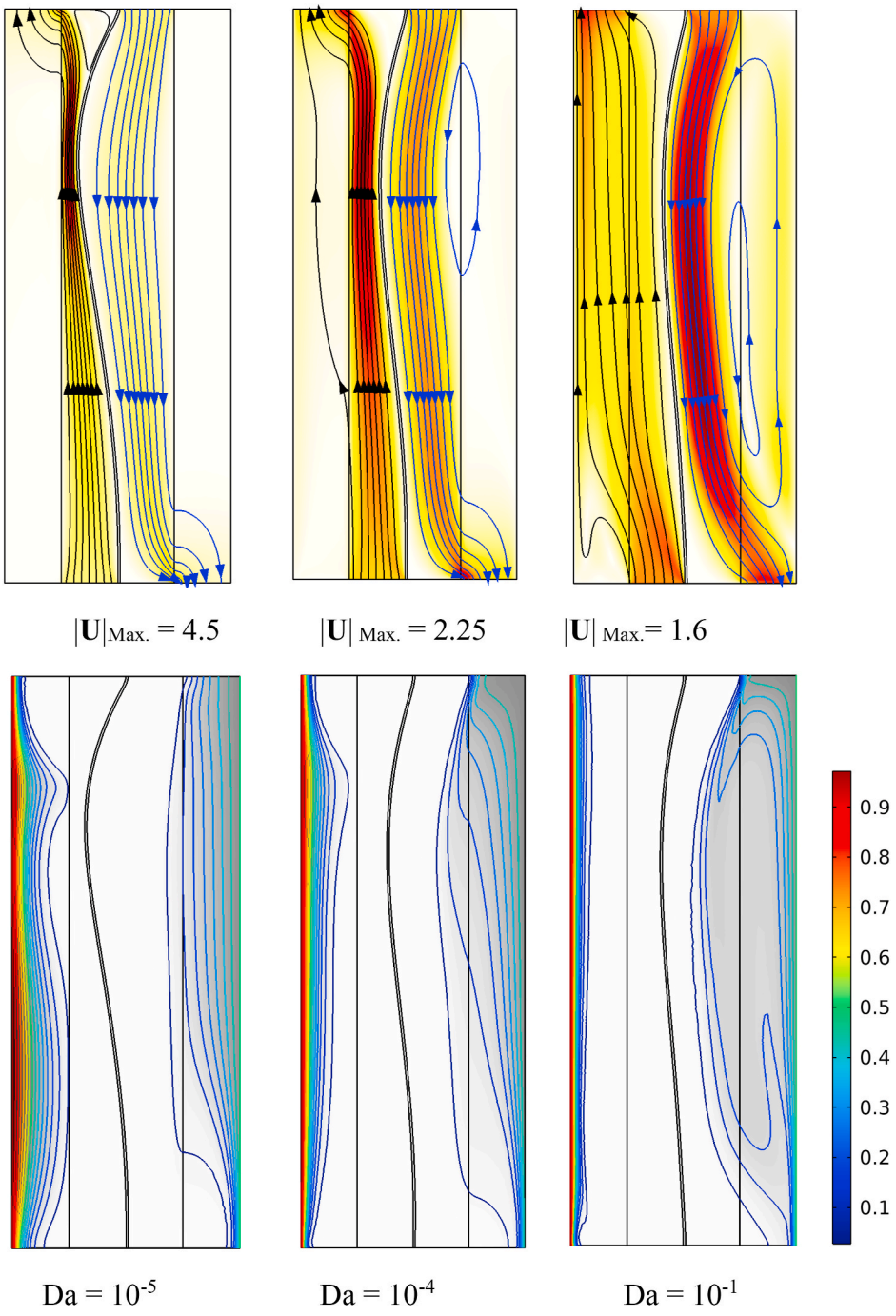

Fig. 8. Streamlines and isotherms for $Re_{II} = 300$, $Re_{III} = 200$, $r_T = 0.5$ and $E = 10^5$.

where F_v is the body force per unit volume acting on the separator, σ_s is the stress tensor and $\mathbf{d_s}$ is the displacement vector of the separator. E is the dimensionless elasticity modulus.

The separator is designated with high thermal conductivity to effectively convey the energy between the two passages; as such, the conduction in the separator is given by:

$$\frac{\partial\theta}{\partial t} = \alpha_r \nabla^2 \theta \tag{6}$$

where $\varphi = 1 - \lambda$, and λ is switched between 1 for the porous layers (I and III) and 0 for the clear passages (II and IV). ε is the porosity of the porous passages. The parameters adopted to cast the original equations into the non-dimensional forms above (equation (1) – (6)) are as follows

$$(U,V) = \frac{(u,v)}{V_{in}}, P = \frac{p}{\rho_f V_{in}^2}, \theta = \frac{(T-T_c)}{(T_{h1}-T_c)}, t = \frac{t^* V_{in}}{w}, r_T = \frac{(T_{h2}-T_c)}{(T_{h1}-T_c)}, (X,Y) = \frac{(x,y)}{w}\ Re = \frac{\rho V_{in} w}{\mu}, Pr = \frac{\mu}{\rho_f \alpha_f}, Da = \frac{K}{w^2}, Ri_j = \frac{Gr_j}{Re_j^2}, Gr_j = \frac{g\beta(T_h - T_c)\, W^3}{\nu_f^2}, E = \frac{\rho_f \left(V_{in}^2\right)_j}{E_s}, Kr = \frac{k_{eff}}{k_f}, \rho_r = \frac{\rho_f}{\rho_s}, \text{and } \alpha_r = \frac{\alpha_s}{\alpha_f}$$

The effective thermal conductivity is estimated by:

$$k_{eff} = k_{sm}(1-\varepsilon) + \varepsilon k_f \tag{7}$$

The drag repressive coefficient in eqns. (2) and (3) is given by (Nield and Bejan., 2017):

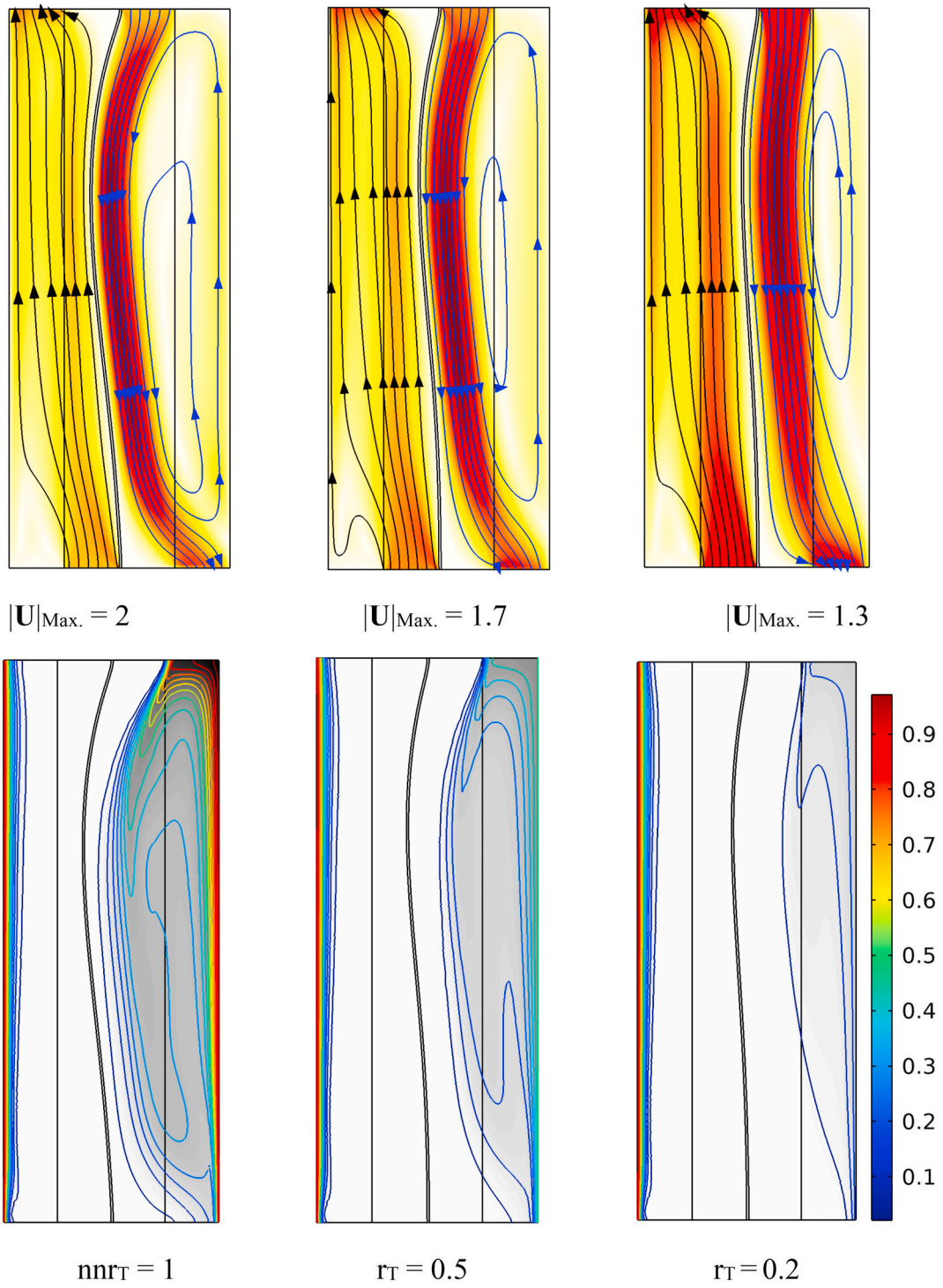

Fig. 9. Streamlines and isotherms for $Re_{II} = 300$, $Re_{III} = 200$, $Da = 10^{-2}$ and $E = 10^{5}$.

$$C_f = \frac{1.75}{\sqrt{150\varepsilon^{3/2}}} \tag{8}$$

The boundary conditions are.

1) Along the interface between regions (I, II) and (III and IV), the following constrains are hold:

$$U, V, \theta|_f = U, V, \theta|_p, \mu_f \left(\frac{\partial U}{\partial Y} + \frac{\partial V}{\partial X}\right)_f = \mu_{eff} \left(\frac{\partial U}{\partial Y} + \frac{\partial V}{\partial X}\right)_p, \theta_f = \theta_p \text{ and } k_f \frac{\partial \theta}{\partial X}\bigg|_f = k_{eff} \frac{\partial \theta}{\partial X}\bigg|_p$$

The effective viscosity of the porous passages μ_{eff} and that of the clear passages μ_f are taken the same based on the Brinkman assumption (Nield and Bejan, 2017).

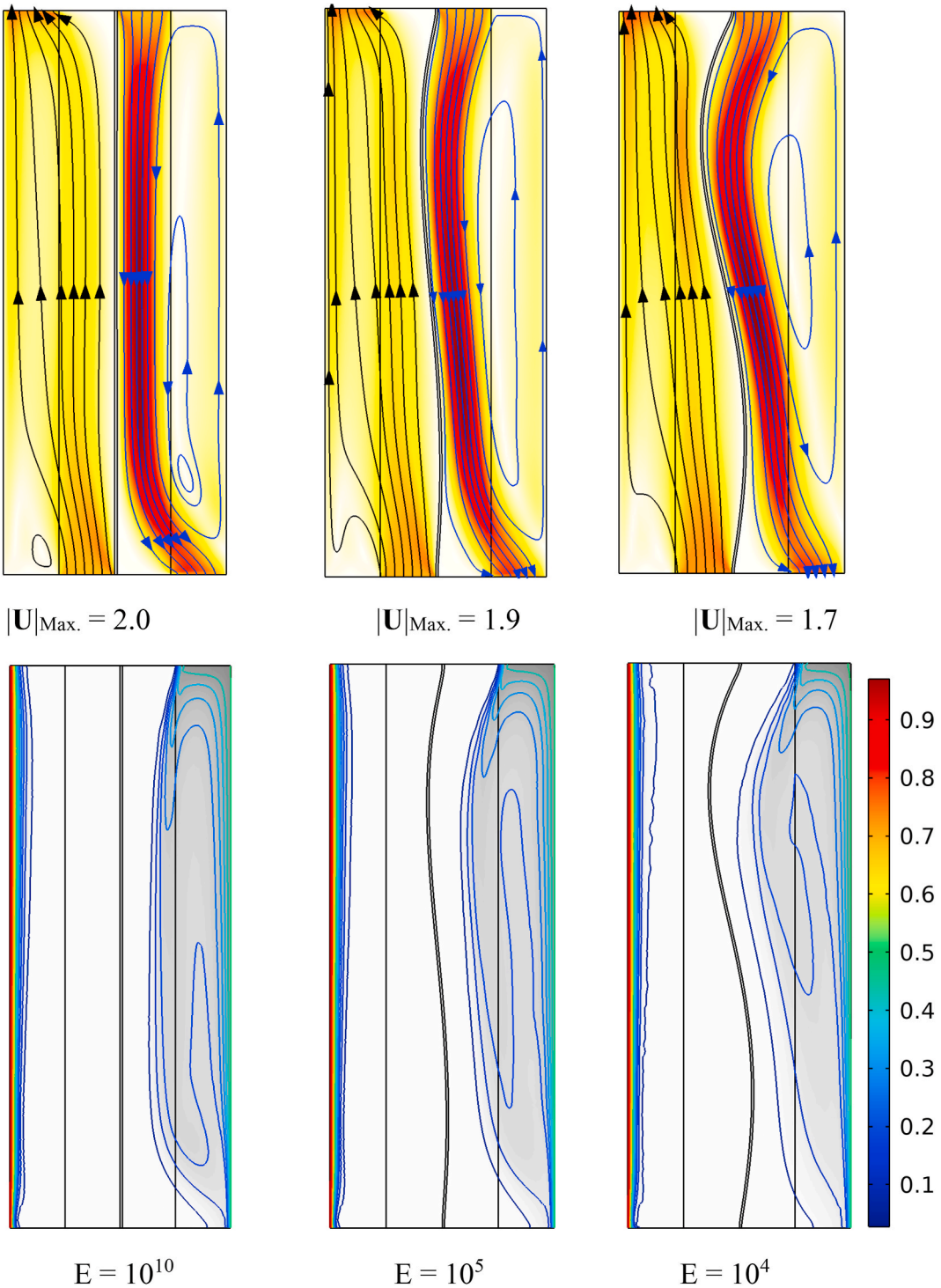

Fig. 10. Streamlines and isotherms for $Re_{II} = 300$, $Re_{III} = 300$, $Da = 10^{-2}$ and $r_T = 0.5$.

2) Along the interface between the separator and regions II and III:

$$\frac{1}{E}\,\sigma_s.\mathbf{n} = -\mathrm{P} + \frac{1}{\mathrm{Re}}\nabla \mathrm{u}, \frac{\partial \boldsymbol{d_s}}{\partial t} = \boldsymbol{u}$$

$$k_f \frac{\partial \theta_f}{\partial \mathbf{n}} = k_s \frac{\partial \theta_s}{\partial \mathbf{n}}$$

3) For the left channel:

$\theta = U = 0$, and $V = +1$ at the inlet of the clear passage.

$P = \frac{\partial U}{\partial Y} = \frac{\partial V}{\partial Y} = \frac{\partial \theta}{\partial Y} = 0$ at the outlet of the porous passage.

4) For the right channel:

$\theta = U = 0$, and $V = -1$ at the inlet of the clear passage.
$P = 0$, $\frac{\partial \theta}{\partial Y} = 0$ at the outlet of the porous passage.

5) Along the left wall, $V = U = 0$ and $\theta = 1$.
6) Along the right wall, $V = U = 0$ and $\theta = r_T$.
7) At the adiabatic ends, $\frac{\partial \theta}{\partial Y} = 0$.

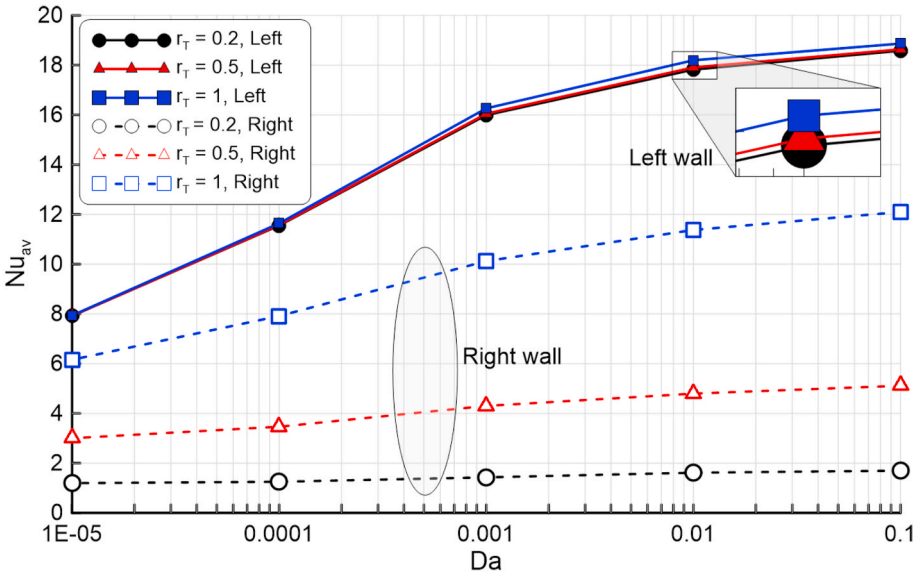

Fig. 11. Nusselt numbers of the right and left walls with Darcy number for several temperature ratios at $Re_{II} = 300$, $Re_{III} = 200$, and $E = 10^5$.

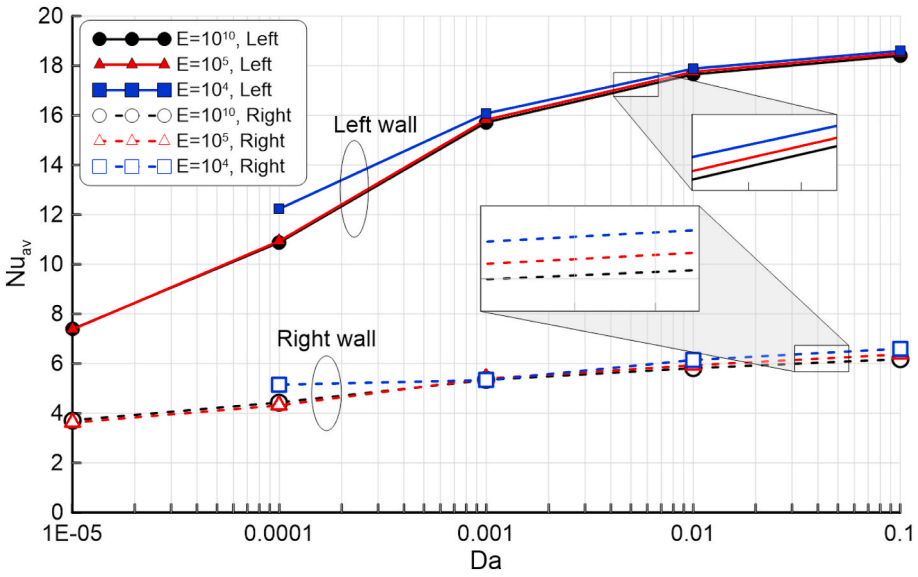

Fig. 12. Nusselt numbers of the right and left walls with Darcy number for several values of elasticity modulus at $Re_{II} = 300$, $Re_{III} = 300$, and $r_T = 0.5$.

The average Nusselt number can be either evaluated on external walls, left or right based on the relation:

$$Nu_{av} = \frac{w}{H}\int_0^{H/w} -\frac{k_{eff}}{k_f}\frac{\partial\theta}{\partial X} \tag{9}$$

To judge the enhanced heat transfer gained by the flexible separator, a performance criterion is adopted based on the ratios of the Nusselt numbers and the pressure drops between the flexible and rigid separator (denoted by subscript "o").

$$PEC = \frac{Nu_{av}/Nu_o}{(f/f_o)^{\frac{1}{3}}} \tag{10}$$

$$f = \frac{2w\Delta p}{\rho V_{in}^2 H} \tag{11}$$

$$\Delta p = -(P_o - P_{in}) \tag{12}$$

3. Numerical manipulation and validations

3.1. Numerical solution

The nomination of the numerical approach in dealing with the complexity brought about by the interaction of the flexible separator and the fluid is a crucial issue. For this task, the sturdy finite element approach (FEM) is chosen. This method allows for a reliable and accurate approximation of the governing equations (1)–(6) by discretizing the overall domain into unstructured triangular elements and rectangular elements close to the no-slip boundaries. The discretization process involves characterizing the overall domain as a compilation of finite elements. These elements are composed of nodes, where nodal approximated functions are assumed. The unknown values within each finite element are then recovered using nodal values. This approach ensures that the distribution of the temperature, velocity and pressure can be accurately interpolated throughout the domain. These basis functions serve as a mathematical representation of the unknowns within each

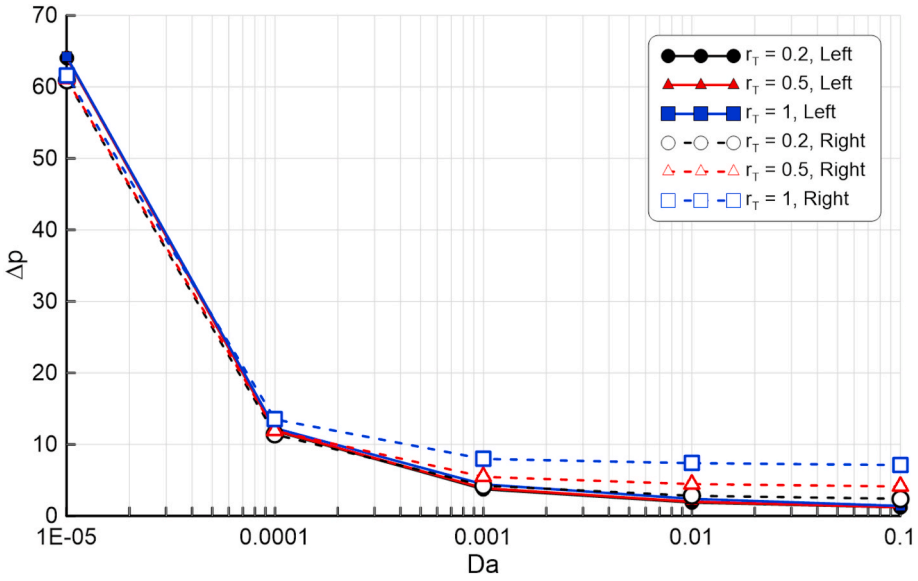

Fig. 13. Pressure drops of the right and left walls with Darcy number for several temperature ratios at $Re_{II} = 300$, $Re_{III} = 200$, and $E = 10^5$.

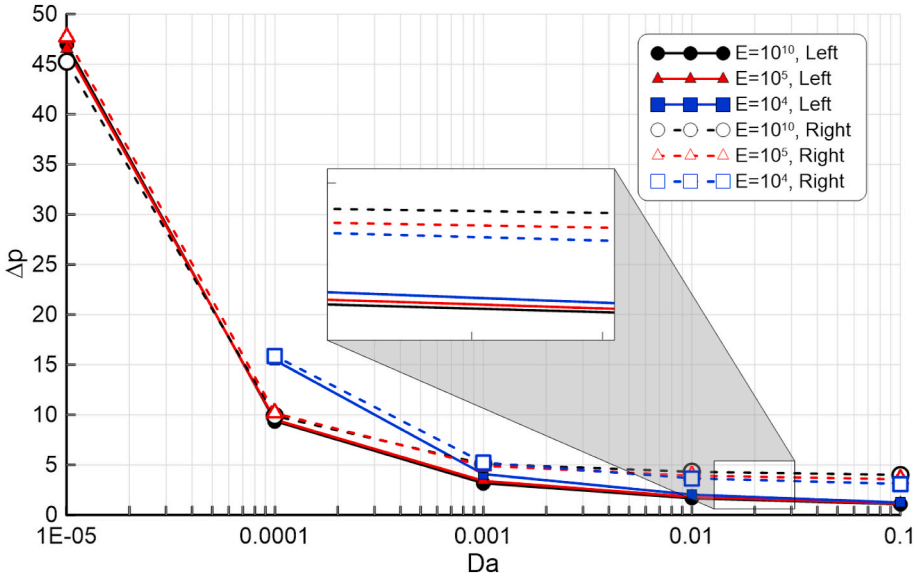

Fig. 14. Pressure drops of the right and left walls with Darcy number for several values of elasticity modulus at $Re_{II} = 300$, $Re_{III} = 300$, and $r_T = 0.5$.

finite element. By selecting appropriate basis functions, it becomes possible to approximate and interpolate the velocity, temperature, and pressure distributions within the computational domain.

The basis function are approximated as

$$\begin{cases} U, V \approx \sum_{i}^{M} (U, V)_i^k \Phi_i^k(x, y) \\ \theta \approx \sum_{i}^{M} \mathrm{T}_i^k \Phi_i^k(x, y) \\ P \approx \sum_{i}^{M} \mathrm{P}_i^k \Phi_i^k(x, y) \end{cases} \tag{13}$$

The subscripts i, k and M denote the node index, time iteration and the number of nodes, respectively. The scheme of Newton-Raphson iteration with a damping factor of 0.80 is employed for solving the residual equations resulting from weighting the residuals of Galerkin FEM. Specifically, residual equations were produced by integrating the weak form of the governing equations across mesh components. A second-order technique was then used to solve these equations. The PARDISO solver (Parallel Direct Solver) (Schenk and Gärtner, 2004; Wriggers, 2008) was used to solve these equations. This solver possesses the merit of solving large numbers of sparse linear equations exploiting the parallel solutions and as a result, significantly reduces the computation time. The step of the non-dimensional time is 0.1.

When the percentage error between two subsequent computations reaches 10^{-6}, the iteration is stopped. Globally, the numerical solution was conducted according to the FSI works. In order to accommodate the deformation of the separator, it is necessary to adjust its numerical domain accordingly. To accomplish this, the arbitrary Lagrangian-Eulerian (ALE) scheme is employed. This algorithm is designed to handle problems involving moving boundaries or interfaces, and it combines elements of both the Lagrangian and Eulerian approaches. This mechanism was illustrated schematically in (Hassan and Ismael, 2023) and intensively in (Donea and Huerta, 2003; Hirt et al., 1974).

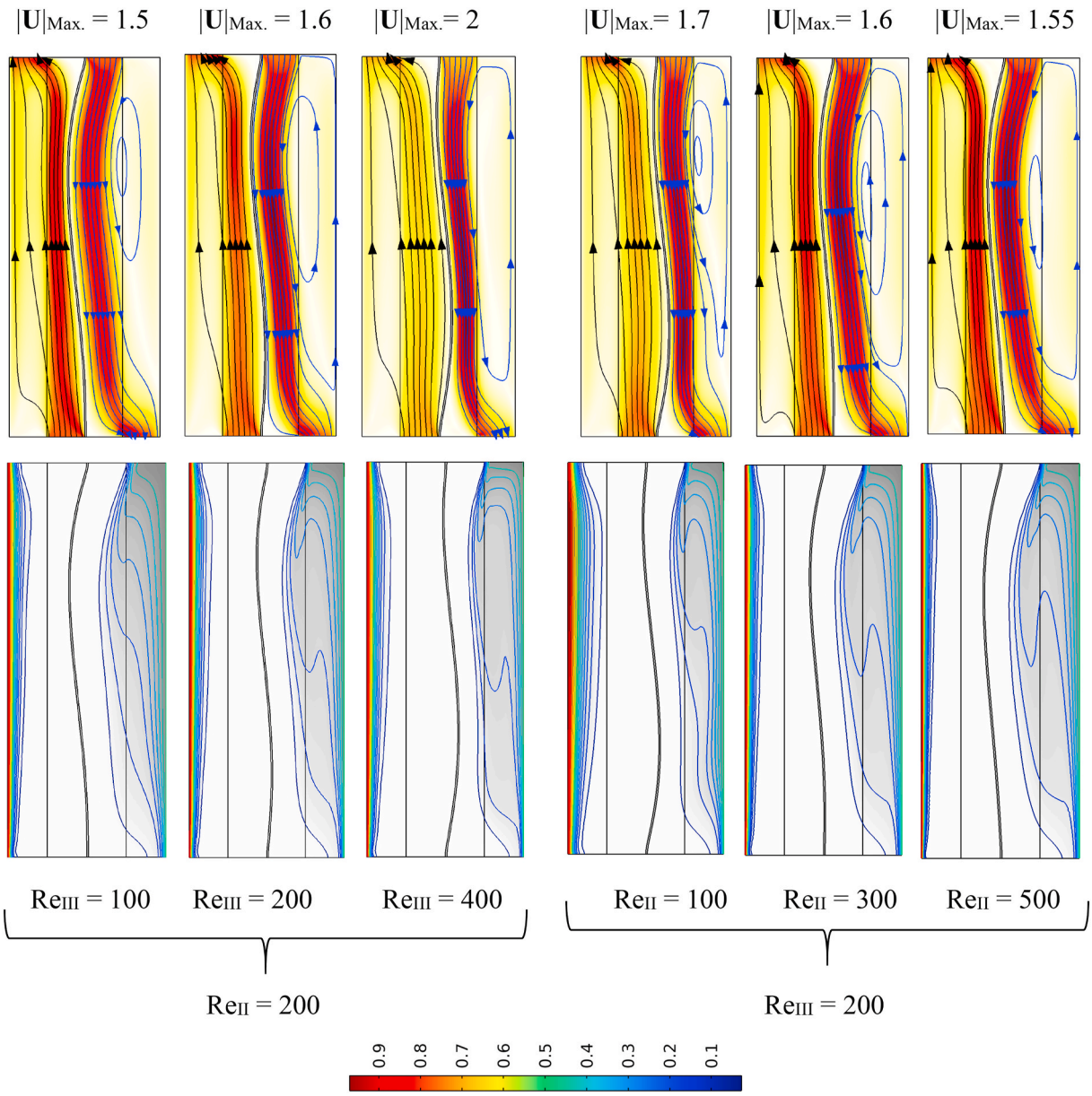

Fig. 15. Streamlines and isotherms for $E = 10^5$, $Da = 10^{-3}$ and $r_T = 0.5$.

3.2. Mesh independence test

To ensure the numerical solution's accuracy, the mesh independence test is not avoidable step. A finer mesh is capable of capturing more details that are intricate and presenting a more precise solution to physical phenomena. However, it is important to note that using an excessively fine mesh can result in unnecessary computational costs without significant improvements in accuracy. In some cases, it may even propagate certain inert singularities. Therefore, it is crucial to determine an appropriate level of refinement that strikes a balance between accuracy and computational efficiency. To achieve this, several mesh sizes were tested and depicted in Fig. 2, which reveals that the numerical solution gets stable beyond the fourth mesh size, namely, 17377 elements, which is adopted in this study. Fig. 3 portrays the distribution and deformation of this mesh (see Table 1).

3.3. Validations

For further assurance of the numerical results, two previous studies are invoked to validate the accuracy of the present numerical solution. The first study by Salah El-Din (2001) who focused on the fully developed flow in a vertical channel divided to two isolated passages using a rigid separator and exposed to constant temperatures. The findings of this study demonstrated a high level of agreement with the Nusselt number as tabulated in Table 2 for two different positions of the separator. Additionally, the upward velocity profiles in each passage also exhibited good agreement, as depicted in Fig. 4.

The second comparison is conducted with the experimental study of Chakraborty et al. (2012), dealing with water flow through a microchannel integrated with an elastic slice as a segment of the top wall of the microchannel. The elastic slice is exposed to two active forces, these are the inertia of water flowing through the channel and an externally applied air pressure on the elastic slice. The amplitudes of the deflected elastic slice are portrayed in Fig. 5 for two circumstances, namely, the deflection of the flexible segment due to flow and external pressure and due to external pressure only. For the two conditions, the current results are in accordance with the experimental results. Hence, trust in the outcomes of the numerical solutions is guaranteed.

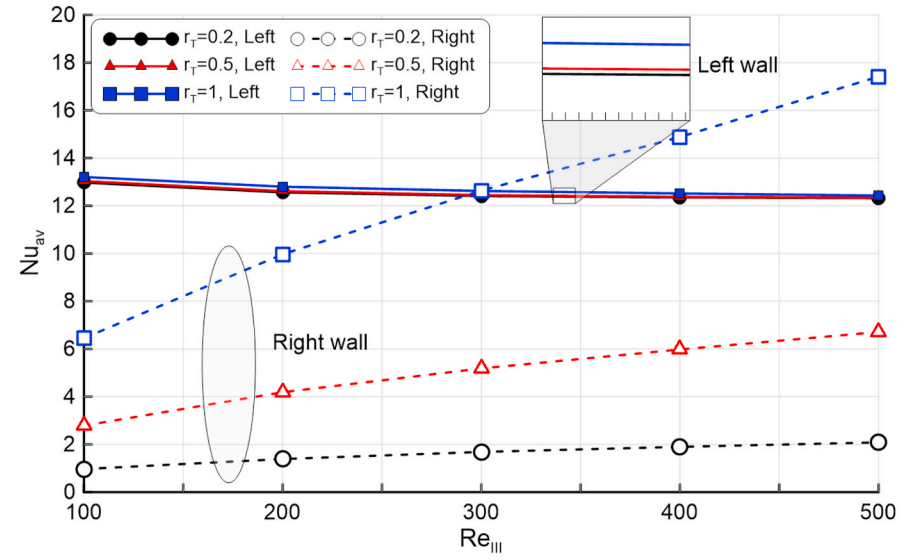

(a) $R_{II} = 200$

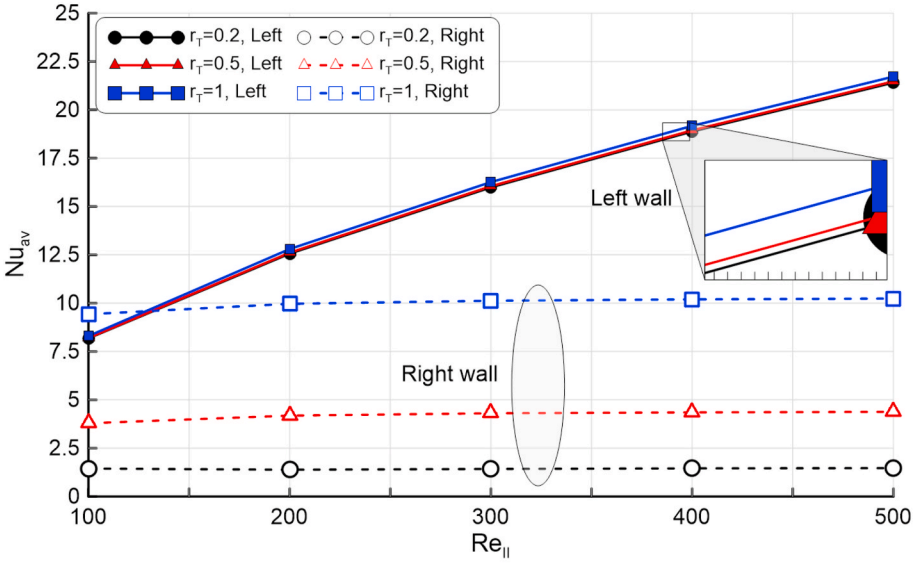

(b) $R_{III} = 200$

Fig. 16. Nusselt numbers of the right and left walls for different r_T values and $E = 10^5$ (a) with the Reynolds number of the right passage and (b) with the Reynolds number of the left passage.

4. Results and discussion

The key parameters of this study are the Darcy number Da, the temperature ratio r_T, the modulus of elasticity E, and the Reynolds number in both passages Re_{II} and Re_{III}. The parameters that are fixed are the porosity $\varepsilon_I = \varepsilon_{IV} = \varepsilon$, Richardson number Ri = 10 (for all regions), and Prandtl number Pr = 6.24. The value of the thermal conductivity of the porous matrix is taken as 0.14 W/m.K which corresponds to PVC beads with a porosity of $\varepsilon = 0.75$. Hence, the conductivity ratio Kr = 0.4947, where the thermal conductivity of water is 0.613 W/m.K. The taken porosity (0.75) is much less than 0.9, therefore the local thermal equilibrium is ensured. The equations are solved transiently to catch the progression of the separator deformation, which is shown in Fig. 6, where a series of times are assessed to determine the time at which the problem reaches the steady state. The figure is produced at $Da = 10^{-4}$ and $E = 10^5$ with $Re_{II} = 200$ and $Re_{III} = 300$. At early time intervals, t = 1–5, the fluid penetrates the right porous layer faster than the left porous layer, which ingests the upward flow beyond t = 10. It is noted that the streamlines and the isotherms stabilize beyond t = 15. The profiles of the deforming separator depicted in Fig. 7 demonstrate that the flexible separator deforms with time up to t = 30, then it stabilizes exactly. Hence, it can be verified that at any time beyond 30, the results are stable; however, all calculations are paid to be at t = 50 to encompass the unexpected variations of the flexible separator with the other ranges of the parameters.

4.1. Impacts of Darcy, elasticity, and the temperature ratio

4.1.1. Thermal and fluid contours

For $Re_{II} = 300$, $Re_{III} = 200$, and $r_T = 0.5$, the influence of the Darcy number is presented in Fig. 8. To understand the physical explanation, it is worth mentioning that the Darcy number reflects the dimensionless permeability of the porous layers which directly affects the flow resistance. Therefore, the figure demonstrates the resistance of the porous

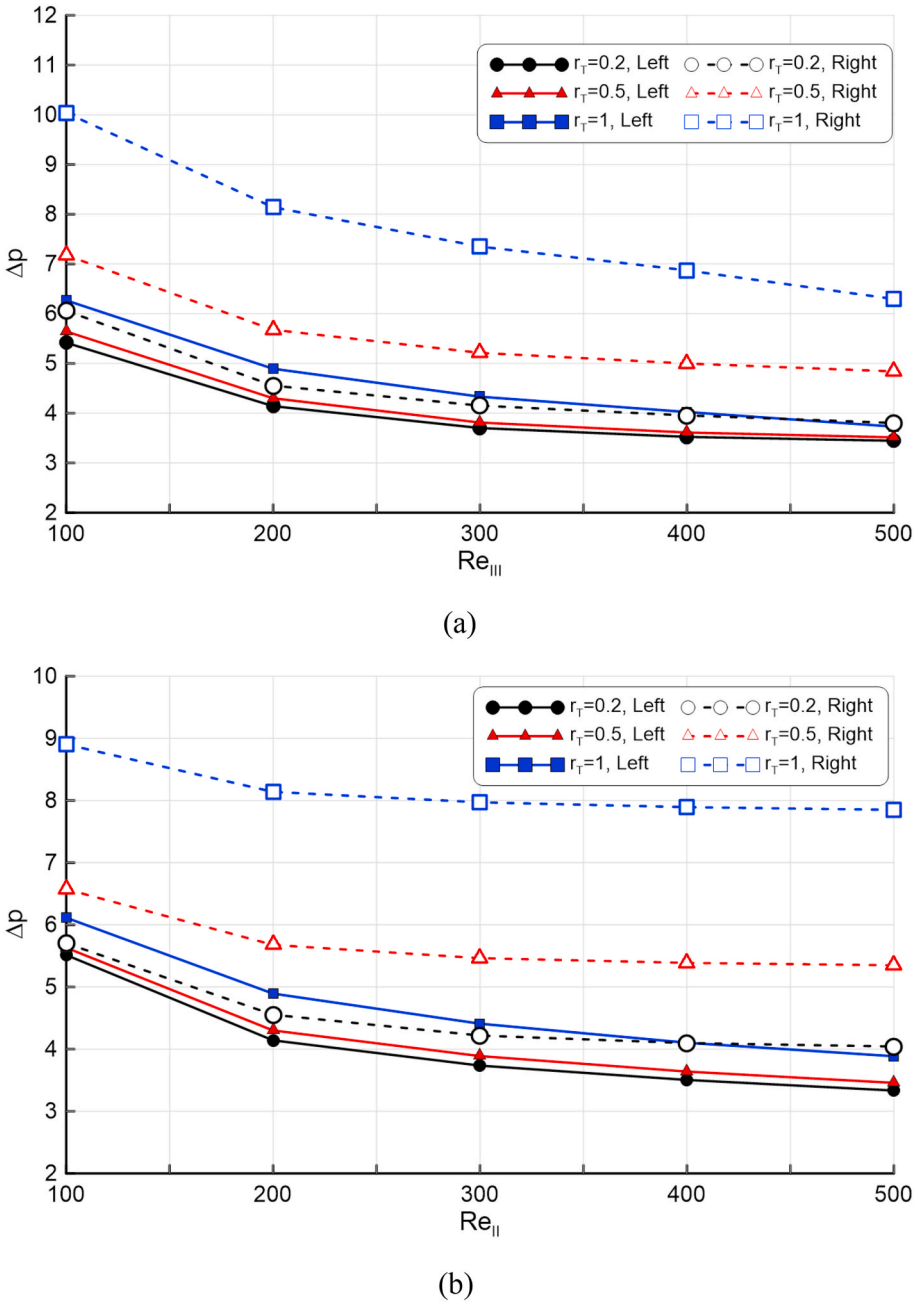

Fig. 17. Pressure drop of the left and right walls for different values of the temperature ratio and $E = 10^5$ (a) with the Reynolds number of the right passage and (b) with the Reynolds number of the left passage.

layers at the lower Darcy number 10^{-5}, where the fluid follows the clear regions while the porous layer appears mostly empty. As Darcy number increases to $Da = 10^{-1}$, the fluid penetrates the porous layers, which manifest less resistance. The figure unveils that at low Darcy number, the separator bends severely towards the higher Reynolds number flow and hence produces a shrinkage path. Thus, the velocity magnitude concentrates at this path, reaching to 2 at $Da = 10^{-5}$ and 1.3 at $Da = 10^{-1}$. Hence, this informs that the concentrated velocity situations suck the separator due to the decrease in the static pressure. This is a very reasonable explanation to why the separator deviates towards the passage having a higher Reynolds number. Noting that the downward flow of the right passage is counter to the rising buoyancy force. Therefore, the buoyancy force and the drag resistance of the porous layer participate and repel the fluid. This generates a vortex at the interface, as shown with $Da = 10^{-4}$ and 10^{-1}. As a sequence of the free permeation of the upward fluid through the porous medium, the isotherms are highly affected by increasing Darcy number, where the thermal boundary layer gets slimmer at $Da = 10^{-1}$. On the other side of the channel, the distribution of the right boundary layer is not appreciably altered with Darcy number.

Fig. 9 portrays that the temperature ratio r_T affects not only the fields of the right passage but also the left passage. This is due to the flexibility of the separator, which is notably observed when $r_T = 1$. The strong buoyancy results in a strengthened vortex, which pushes the separator towards the left and leads to greater velocity close to the bend portion. As r_T is reduced, the buoyancy force decreases. Consequently, the interface recirculation shrinks, which mitigates the fluid force on the separator, resulting in less deformation, as shown with $r_T = 0.2$. Although the isotherms of the left passage exhibit marginal variation with r_T, the boundary layer of the right passage is distinct when $r_T = 1$

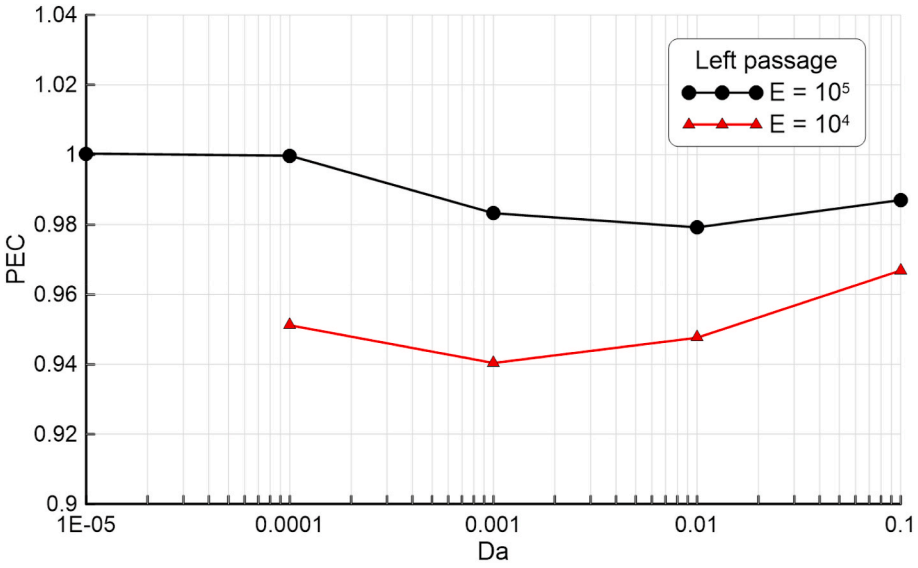

(a)

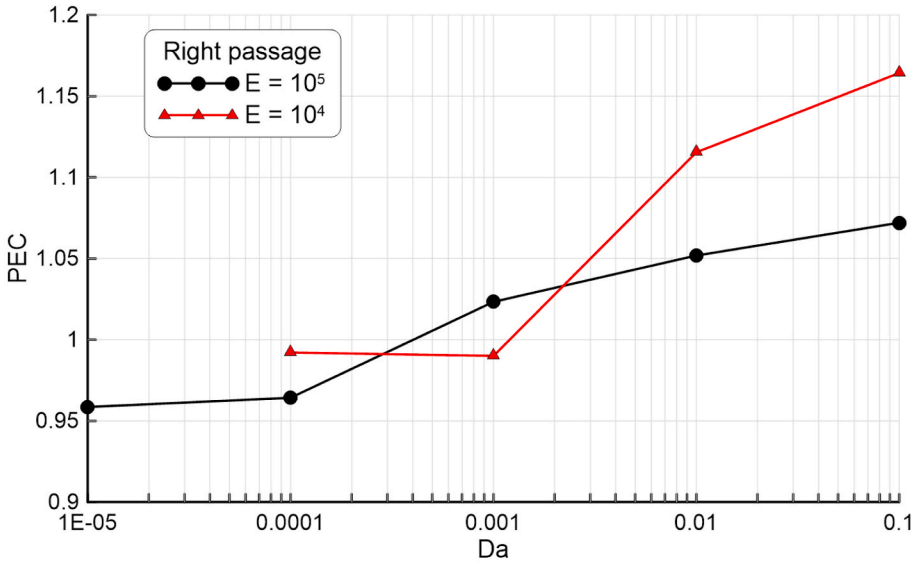

(b)

Fig. 18. Performance criterion for $R_I = R_{III} = 300$ and $r_T = 0.5$, (a) the left passage and (b) the right passage.

and indistinct when $r_T = 0.5$ and 0.2.

The variations of the elasticity modulus of the separator affect the streamlines and the isotherms as portrayed in Fig. 10 for equivalent Reynolds numbers $Re_{II} = Re_{III} = 300$, $Da = 10^{-2}$, and $r_T = 0.5$. All passages are straight when $E = 10^{10}$ as an indication to the separator's rigidity. The separator deforms symmetrically within $E \leq 10^5$, where the flow energy is sufficient to strain the separator. The almost symmetric deformation of the separator is due to the equivalent Reynolds number leading to an S-shaped separator at $E = 10^4$. The S-shaped deformation squeezes the upward flow close to the exit, directing the flow towards the porous layer. On the other hand, the core of the interface circulation is lifted with decreasing E. The velocity magnitude is maximum when the separator is rigid ($E = 10^{10}$) as most fluid passes through the clear layers in this case. The isotherms of the left passage manifest minor variation with E, where a thin boundary layer adjoins the left hotter wall, while the right boundary layer propagates and is harmonic with the separator.

4.1.2. Nusselt number and pressure drop

The Nusselt numbers of the hotter (left) wall and of the hot (right) wall exhibit different increasing rates with Darcy number as presented in Fig. 11. For a given value of r_T equal to 1, the left wall Nusselt number elevates by 138%, while at the right wall, it elevates by 96%. As was observed in the previous contours, the buoyancy force encounters the downward flow of the right passage; therefore, this hampers the momentum exchange and hence reduces the Nusselt number. Contrarily, in the left passage, the upward flow is assisted by the buoyancy force, which promotes the elevation of the Nusselt number. Furthermore, the figure also unveils the influence of r_T, which is marginal on the left wall and significant on the right wall. Lifting r_T from 0.2 to 1, the right Nusselt number at Darcy = 0.01 elevates by 604%, while the left wall Nusselt number promotes by 2% only. This is a postulated result because the r_T mainly affects the right passage. In the same regard, Fig. 12 illustrates the impact of the modulus of elasticity E of the separator for $r_T = 0.5$ and $Re_{II} = Re_{III} = 300$. The figure shows that the modulus of

elasticity becomes influential at lower permeability layers, where at Da $= 10^{-4}$, the left Nusselt number elevates by about 10.4 % while the right one increases by 16.25% when the flexibility of the separator is modulated from E $= 10^{10}$ to 10^5. This is because the deformed separator creates a wavy passage that augments the momentum exchange. It is worth mentioning that at E $= 10^4$, the solution is impossible with Da $= 10^5$ because the strain of the separator exceeds the clear domains and touches the interface of the porous layers.

Noting that the pressure drop curves in Figs. 13 and 14, it is asserted that the higher permeability (higher Da number) porous layer provides free paths to the flow, hence reducing the pressure drop notably. Due to the encountered actions of the downward flow and the buoyancy force, the right passage experienced a greater pressure drop than the left passage. Fig. 14 shows an increase in the pressure drop with E $= 10^{4,}$ i.e., with the elastic separator. This is because the wavy passages add extra contact area between the fluid and the separator surface.

4.2. The impact of passages Reynolds number

In Fig. 15, the Reynolds numbers are varied alternatively between the two passages to enrich the understanding of their roles. The figure demonstrates what is noted in Fig. 8, namely, the separator deforms towards the passage of a higher Reynolds number, and we attributed this phenomenon to the decrease of the static pressure. The figure also demonstrates the symmetric deformation of the separator (S-shaped) for equivalent Reynolds numbers, depicted in Fig. 15 (a) for $Re_{II} = Re_{III} = 200$. However, the figure discovers the following additional findings: (i) the maximum velocity magnitude occurs when the separator deviates towards the right porous layer that exerts a drag against the downward flow and hence traps the flow in the concentrated situations. As a result, the velocity magnitude increases with increasing Re_{III} and decreases with increasing Re_{II}. (ii) Varying of either Reynolds numbers, the vortex of the right interface is influenced consequently. The isotherms depict thinning boundary layers as their corresponding Reynolds number is increased. Therefore, for a fixed Re_{II}, the right wall Nusselt number elevates with $Re_{III,}$ as given in Fig. 16 (a). The percentage increase of Nu_{av} is highly affected by the r_T, where elevating Re_{III} from 100 to 500, Nu_{av} elevates by 116% and 170% for $r_T = 0.2$ and 1.0, respectively. On the other hand, Fig. 16 (b) presents the rise of Nu_{av} of the left wall with Re_{II} irrespectively to the r_T.

It is well-established that a reduction in viscous effects leads to a corresponding decrease in frictional losses. This phenomenon can be quantitatively described by an increase in the Reynolds number, showing how much inertial force there is compared to viscous force in a fluid flow. Fig. 17 (a) and (b) corroborate this principle, showing that the pressure drop across both passages diminishes as their respective Reynolds numbers increase. These figures also highlight the crucial role of the flexible separator in the system. Specifically, for a given Reynolds number for, say, the left passage (as shown in Fig. 15(a)), an increase in Reynolds number for the right passage (Re_{III}) causes the flexible separator to shift towards the right. This action effectively enlarges the cross-sectional area of the left passage (with a fixed Reynolds number, Re_I), thereby reducing the fluid velocity and, consequently, mitigating the pressure drop in that passage. Notably, due to the counter-flow mechanism inherent in this setup, the pressure drop in the right passage consistently exceeds that in the left passage.

4.3. Overall performance

The merit of the performance criterion explained in equation (10) is to provide an overview of the competition between the enhanced energy transmission and the friction effect for a given reference parameter. In this study, the rigid separator was taken as a reference case. Fig. 18 (a) and (b) present the performance criterion (PEC) for both passages at $r_T = 0.5$ and $Re_I = Re_{III} = 300$. For the left aiding channel, the elastic wall affects the performance adversely, where PEC is less than unity for most ranges of the Darcy number, especially at a high elasticity separator (E $= 10^4$). The process of the heat exchange in the right channel, on the other hand, exhibits a promising performance where the PEC is greater than unity for Da $\geq 10^{-3}$, especially for the high elasticity separator. Hence, it is deduced that the elastic separator can promote the overall performance of heat exchange in encountered vertical flow through a layered channel.

5. Conclusions

The current paper investigates the energy transmission and counter flow through a double-passage channel of a flexible separator. Each passage involves clear and porous layers. The upward flow of the left passage coincides with the buoyancy force, while in the right passage, the downward flow is opposite the buoyancy force. The inlet flows are colder than the different heating walls. FSI coupled with FEM are utilized in solving the problem. The acquired results are based on varying the Darcy number, the elasticity of the separator, Reynolds number, and the temperature ratio. The following remarks are deduced:

(i) The strain energy stored in the elastic separator augments the Nusselt number but slightly increases the pressure drop. Even though it promotes the performance of the heat exchange in the double-passages vertical partially layered channel.
(ii) The elasticity modulus of the separator emerges when the porous layers possess lower permeability, where at Da $= 10^{-4}$, the left wall Nusselt number elevates by 10.4% while that of the right wall by 16.25% when the separator is switched from rigid (E $= 10^{10}$) to a flexible one (E $= 10^5$).
(iii) In most cases, the left wall Nusselt number is higher than that of the right wall; this is because of the aiding buoyancy within the left passage and encountered buoyancy within the right passage.
(iv) The high permeability porous layer (high Darcy number) promotes the Nusselt number; for example the latter increases by 138% for the left wall and by 96% for the right wall when the Darcy number is increased from 10^{-5} to 10^{-1}.
(v) The temperature ratio affects the right wall Nusselt number significantly, while its effect is marginal on the left wall. At Da $= 10^{-2}$, raising the temperature ratio from 0.2 to 1.0, the right wall Nusselt number increases by about 600% while the left wall Nusselt number increases only by 2%.
(vi) Increasing the Reynolds number of each passage enhances the corresponding Nusselt number. However, the separator assumes a symmetric S-shaped when the Reynolds numbers of the two passages are equivalent.
(vii) Based on the performance criterion, the best design of the present problem is being with a high separator flexibility (E $= 10^4$), higher Darcy number (Da $\geq 10^{-3}$) and the flow is being opposed to the buoyancy direction (downward flow).

We are cognizant that our paper may have two limitations. These are the laminar flow regimes and the uniform porosity of the porous layers. Future studies should address the role of the flexible separator in turbulent flow and variable porosity passages.

CRediT authorship contribution statement

Muneer Ismael: Conceptualization, Formal analysis, Investigation, Methodology, Supervision. **Mohammad Ghalambaz:** Formal analysis, Investigation, Resources, Visualization, Writing – review & editing. **Zehba Raizah:** Resources, Visualization, Writing – review & editing. **Mehdi Fteiti:** Data curation, Resources, Visualization, Writing – review & editing.

Declaration of competing interest

The authors declare that they have no known competing financial interests or personal relationships that could have appeared to influence the work reported in this paper.

Data availability

Data will be made available on request.

Acknowledgements

The authors would like to thank the Deanship of Scientific Research at Umm Al-Qura University for supporting this work by Grant Code: (23UQU4310414DSR011). The authors extend their appreciation to the Deanship of Research and Graduate Studies at King Khalid University for funding this work through large Research Group Project under the grant number (RGP2/194/45). This research of Mohammad Ghalambaz was supported by the Tomsk State University Development Programme (Priority-2030). The corresponding author (Muneer A. Ismael) extends his thanks to University of Warith Al-Anbiyaa, Iraq for financial support for this study.

Appendix A. Supplementary data

Supplementary data to this article can be found online at https://doi.org/10.1016/j.oceaneng.2024.118008.

References

Athal, I., Sarris, I.E., Velusamy, P., Govindan, V., 2023. Viscosity dissipation and mixed convection flow in a vertical double-passage channel with permeable fluid. Front. Nanotechnol. 4, 1058973.
Athith, T., Trilok, G., Jadhav, P.H., Gnanasekaran, N., 2022. Heat transfer optimization using genetic algorithm and artificial neural network in a heat exchanger with partially filled different high porosity metal foam. Mater. Today: Proc. 51, 1642–1648.
Biswas, N., Mahapatra, P.S., Manna, N.K., 2015. Thermal management of heating element in a ventilated enclosure. Int. Commun. Heat Mass Tran. 66, 84–92.
Biswas, N., Chamkha, A.J., Manna, N.K., 2020a. Energy-saving method of heat transfer enhancement during magneto-thermal convection in typical thermal cavities adopting aspiration. SN Appl. Sci. 2, 1–25.
Biswas, N., Manna, N.K., Datta, A., Mandal, D.K., Benim, A.C., 2020b. Role of aspiration to enhance MHD convection in protruded heater cavity. Prog. Comput. Fluid Dynam. Int. J. 20 (6), 363–378.
Chakraborty, D., Prakash, J.R., Friend, J., Yeo, L., 2012. Fluid-structure interaction in deformable microchannels. Phys. Fluids 24 (10).
Chen, T., Wang, Y., Qi, C., Chen, L., Tang, Z., 2022. Effects of metal foam filling heights and tilt angles on the cooling performance of a heat sink filled with nanofluids. Int. Commun. Heat Mass Tran. 138, 106326.
Cheng, C.-H., Kou, H.-S., Huang, W.-H., 1989. Laminar fully developed forced-convection flow within an asymmetrically heated horizontal double-passage channel. Appl. Energy 33 (4), 265–286.
Donea, J., Huerta, A., 2003. Finite Element Methods for Flow Problems. John Wiley & Sons.
Fteiti, M.A., Ghalambaz, M., Younis, O., Sheremet, M., Ismael, M., 2023. The influence of the metal foam layer shape on the thermal charging response time of a latent heat thermal energy storage system. J. Energy Storage 58, 106284.
Ghalambaz, M., Mahdi, J.M., Shafaghat, A., Eisapour, A.H., Younis, O., Talebizadeh Sardari, P., Yaïci, W., 2021. Effect of twisted fin array in a triple-tube latent heat storage system during the charging mode. Sustainability 13 (5), 2685.
Girish, N., Sankar, M., 2020. Fully developed mixed convection in vertical double passage porous annuli. In: Journal of Physics: Conference Series. IOP Publishing, 012050.
Girish, N., Makinde, O.D., Sankar, M., 2018. Numerical investigation of developing natural convection in vertical double-passage porous annuli. In: Defect and Diffusion Forum. Trans Tech Publ, pp. 442–460.
Hassan, A.A., Ismael, M.A., 2023. Fluid-structure interaction of a sweeping impingement jet for cooling hot flat target. Int. J. Therm. Sci. 190, 108323.
Hazra, C., Biswas, N., Manna, N.K., 2020. Thermal magneto-hydrodynamics in a ventilated porous enclosure. Sādhanā 45 (1), 224.
Hirt, C.W., Amsden, A.A., Cook, J., 1974. An arbitrary Lagrangian-Eulerian computing method for all flow speeds. J. Comput. Phys. 14 (3), 227–253.
Hoseini, S.S., Seyedkanani, A., Najafi, G., Sasmito, A.P., Akbarzadeh, A., 2023. Multiscale architected porous materials for renewable energy conversion and storage. Energy Storage Mater., 102768
Ismael, M.A., Hussain, S., Alsabery, A.I., Chamkha, A.J., Hashim, I., 2022. Thermal performance of a vertical double-passage channel separated by a flexible thin sheet. Int. Commun. Heat Mass Tran. 137, 106238.
Jadhav, P.H., Trilok, G., Gnanasekaran, N., Mobedi, M., 2022. Performance score based multi-objective optimization for thermal design of partially filled high porosity metal foam pipes under forced convection. Int. J. Heat Mass Tran. 182, 121911.
Jadhav, P.H., Gnanasekaran, N., Mobedi, M., 2023. Analysis of functionally graded metal foams for the accomplishment of heat transfer enhancement under partially filled condition in a heat exchanger. Energy 263, 125691.
Khanafer, K., Vafai, K., 2020. Effect of a circular cylinder and flexible wall on natural convective heat transfer characteristics in a cavity filled with a porous medium. Appl. Therm. Eng. 181, 115989.
Kumar, J.P., Umavathi, J., Prema, H., 2011. Free convection of Walter's fluid flow in a vertical double-passage wavy channel with heat source. Int. J. Eng. Sci. Technol. 3 (1).
Lori, M.S., Vafai, K., 2022. Heat transfer and fluid flow analysis of microchannel heat sinks with periodic vertical porous ribs. Appl. Therm. Eng. 205, 118059.
Nield, D.A., Bejan, A., 2017. Convection in Porous Media, fifth ed. Springer, New York. 2017.
Obata, M., Yamaga, J., Taniguchi, H., 1989. Heat transfer characteristics of a return-flow steam-cooled gas turbine blade. Exp. Therm. Fluid Sci. 2 (3), 323–332.
Pantua, C.A.J., Calautit, J.K., Wu, Y., 2020. A fluid-structure interaction (FSI) and energy generation modelling for roof mounted renewable energy installations in buildings for extreme weather and typhoon resilience. Renew. Energy 160, 770–787.
Pratap Kumar, J., Umavathi, J.C., Metri, P.G., Silvestrov, S., 2016. Effect of first order chemical reaction on magneto convection in a vertical double passage channel, Engineering Mathematics I: electromagnetics, Fluid Mechanics. In: Material Physics and Financial Engineering. Springer, pp. 247–279.
Salah El-Din, M., 1994. Fully developed laminar convection in a vertical double-passage channel. Appl. Energy 47 (1), 69–75.
Salah El-Din, M., 2001. Developing laminar convection in a vertical double-passage channel. Heat Mass Tran. 38 (1), 93–96.
Salah El-Din, M., 2002. Effect of viscous dissipation on fully developed laminar mixed convection in a vertical double-passage channel. Int. J. Therm. Sci. 41 (3), 253–259.
Sankar, M., Girish, N., Siri, Z., 2018. Fully developed magnetoconvective heat transfer in vertical double-passage porous annuli. Flow Transport Subsurf. Environ. 217–249.
Schenk, O., Gärtner, K., 2004. Solving unsymmetric sparse systems of linear equations with PARDISO. Future Generat. Comput. Syst. 20 (3), 475–487.
Selimefendigil, F., Öztop, H.F., 2016a. Analysis of MHD mixed convection in a flexible walled and nanofluids filled lid-driven cavity with volumetric heat generation. Int. J. Mech. Sci. 118, 113–124.
Selimefendigil, F., Öztop, H.F., 2016b. Natural convection in a flexible sided triangular cavity with internal heat generation under the effect of inclined magnetic field. J. Magn. Magn Mater. 417, 327–337.
Selimefendigil, F., Öztop, H.F., 2017. Mixed convection in a partially heated triangular cavity filled with nanofluid having a partially flexible wall and internal heat generation. J. Taiwan Inst. Chem. Eng. 70, 168–178.
Selimefendigil, F., Öztop, H.F., Abu-Hamdeh, N., 2016. Mixed convection due to rotating cylinder in an internally heated and flexible walled cavity filled with SiO2–water nanofluids: effect of nanoparticle shape. Int. Commun. Heat Mass Tran. 71, 9–19.
Selimefendigil, F., Öztop, H.F., Chamkha, A.J., 2017. Analysis of mixed convection of nanofluid in a 3D lid-driven trapezoidal cavity with flexible side surfaces and inner cylinder. Int. Commun. Heat Mass Tran. 87, 40–51.
Selimefendigil, F., Oztop, H.F., Chamkha, A.J., 2019. MHD mixed convection in a nanofluid filled vertical lid-driven cavity having a flexible fin attached to its upper wall. J. Therm. Anal. Calorim. 135, 325–340.
Slimani, M.E.A., Amirat, M., Bahria, S., 2015. Study and modeling of heat transfer and energy performance in a hybrid PV/T collector with double passage of air. Int. J. Energy a Clean Environ. (IJECE) 16 (1–4).
Umavathi, J.C., Kumar, J.P., Sheremet, M.A., 2017. Heat and mass transfer in a vertical double passage channel filled with electrically conducting fluid. Phys. Stat. Mech. Appl. 465, 195–216.
Vijayaraghavan, S., Shah, R., Kumar, D.V., 2022. A comparison study on thermal performance enhancement of corrugated oil cooler with internal turbulators–Numerical and experimental approach. Mater. Today: Proc. 52, 642–648.
Wriggers, P., 2008. Nonlinear Finite Element Methods. Springer Science & Business Media.